Supporting Information: Imaging Photonic Resonances within an All-Dielectric Metasurface via Photoelectron Emission Microscopy

Authors:

*Andrew R. Kim, Chloe F. Doiron, Fernando J. Vega, Jaeyeon Yu, Alex M. Boehm, Joseph P. Klesko, Igal Brener, Raktim Sarma, Alexander Cerjan, Taisuke Ohta**

PEEM data processing:

We processed the PEEM images to eliminate the impacts of (1) the two-dimensional electron detector's inhomogeneous response, (2) the image distortion originating from the imperfect alignment of the electron optics, (3) the varying laser power at each photon energy (E_{ph}), and (4) the dependence of photoemission yield (PEY) on E_{ph}. For (1), we first acquired an image of an area where the sample surface is homogeneous. This reference image was used to correct the inhomogeneous response of the electron detector. To eliminate the image distortion in (2), we aligned the meta-atom arrays as if the meta-atom locations form a perfectly orthogonal grid. We found that the distortion within the field of view amounts as much as 20 pixels within a 600 pixel × 600 pixel image (with ~25 nm/pixel) depending on the alignment of the electron optics and the position within the detector area, with the most severe distortion occurring near the edges of the detector. For (3), we kept the exposure time of the detector constant for all data presented and normalized each image for laser power by dividing by the square of the power [to account for 2-photon photoemission (2PPE) process][1,2,3] recorded for the image. Finally, to normalize image intensity for (4), we measured the 2PPE PEY of a 46 nm-thick TiO_2 thin film as a function of wavelength [Figure S1(b)]. We fitted a spline function to the PEY data and used the fitted function to normalize the PEEM data.

To further improve signal-to-noise ratio as well as to reduce the impact of imperfections in individual meta-atoms, we averaged over multiple unit cells to form an "accumulated meta-atom" image as shown in Figure S4. Figure S4(a) is the PEEM image of the metasurface (E_{ph} of 2.7 eV, 0° polarization) showing the individual meta-atoms without accumulation. The colored boxes surround the grid of 36 unit cells used to form the accumulated meta-atoms in Figure S4(b) highlighted by the same colored boxes. We limited accumulation to unit cells at least 8 cells away from the edge of the array to eliminate any effect from the broken translational symmetry.[4]

To correct nontrivial sample drift due to fluctuations within the instrument (thermal, electrical, etc.), we manually aligned each PEEM image relative to each other. Alignment was performed with assistance from reference images taken by the deep-UV incoherent light source (described in PEEM imaging in Methods section in main text), which produces a photoemission intensity map that corresponds to the shape of the meta-atom because it does not excite a resonant response. Figure S5 shows an example of the reference image, where (a) is the PEEM image of a unit cell at photon energy of 2.76 eV for 0° polarization and (b) is the same unit cell illuminated

by the deep-UV incoherent light source of 6.20 eV. Figure S5(c) is a diagram of the unit cell, with the white circle representing the meta-atom interior and the black area representing the exterior. We see that the intensity distribution in Figure S5(b) more closely resembles the shape of the meta-atom in Figure S5(c) (white circle). By taking reference images immediately after taking an image at a chosen SHG wavelength, we determine where the field patterns are located with respect to the meta-atom.

MEEP simulation:

The finite-difference time-domain simulation method used for all simulations in the main text was performed via the Python package, MIT Electromagnetic Equation Propagation (MEEP).[5] The simulation output consists of the electric (or magnetic) field distribution within the simulated volume (can be a unit cell or the entire system if not periodic) for a given moment in time. In this section, we describe how the simulated, three-dimensional electric field distribution volume (FDV) from MEEP is processed to form the two-dimensional (x-y plane) image that is analogous to PEEM images.

Since photoemission occurs at all points in time when an electric field exists in the host material, a single PEEM image (whose exposure time of ~1 s is much larger than the pulse duration of UV-vis light source) accumulates photoelectrons throughout the full optical response of the metasurface. Therefore, we calculate the electric FDV at multiple points in time, beginning with when the illuminating light source (gaussian plane wave) reaches the metasurface and ending when the resulting fields have decayed (defined 15 standard deviations of the gaussian plane wave after the start). To account for the 2PPE process, which depends on the fourth power of the electric field, or $|\boldsymbol{E}|^4$, the electric FDV is raised to the fourth power to produce the $|\boldsymbol{E}|^4$ FDV. To reduce computational burden, we integrate in discrete time steps of 5/8 of an oscillation period, i.e., each FDV is separated in time by 5/8 of a period. This time step converges similarly to integrating in time steps of 1/8 period while reducing total simulation runtime. Figure S6 plots the intensity spectra from simulated images of one unit cell [taken similarly to those shown in Figure 4(c) and (d)] for integration in time steps of 5/8, 1/4, and 1/8 period. All three are very similar and overlap with each other: the 1/4 period spectrum diverges slightly at E_{ph} of ~2.73 eV and below, while the 5/8 and 1/8 period spectra stay overlapped. Thus, by integrating the $|\boldsymbol{E}|^4$ FDV in time steps of 5/8 of an oscillation period, we produce results analogous to the temporal integration in PEEM imaging.

As described by Figure 2 in the main text, the temporally integrated $|\boldsymbol{E}|^4$ FDV is processed using the electron inelastic mean free path (IMFP) to replicate the effect of IMFP on the photoemission intensity imaged by PEEM. We reiterate the process above in more detail as described in the following. As illustrated in Figure 2(b), the $|\boldsymbol{E}|^4$ FDV is divided into 2-dimensional slices that contain the $|\boldsymbol{E}|^4$ distribution in the x-y plane as a function of height (z direction). The spacing between each slice is 2.5 nm. Each pixel (~8.8 × 8.8 nm^2 size) in each slice is further divided into a grid of 7×7 subpixels, and the subpixel values are modified from the parent pixel's value according to the subpixel's spatial position. If the subpixel lies within vacuum, its value is set to

zero; if the subpixel lies within the host material, then its depth D from the host material's surface (which is either the top of the meta-atom or the top of the ALD TiO_2 layer) is calculated. The intensity of the subpixel I is then attenuated according to the electron IMFP λ, as in $I(D) \propto e^{-D/\lambda}$ [Figure 2(c) shows the attenuation curve as a function of depth D]. Off-surface normal emission of the photoelectrons was not considered to simplify the calculations.

In addition to processing for IMFP, the subpixels are further processed for the difference in PEY between the TiO_2 metasurface and SiO_2 substrate based on the empirical photoemission intensity ratio. Figure S2 plots the PEY ratio (along with a spline fit) as a function of wavelength determined by a photon energy scan of thin films (46 nm thick for TiO_2, and 54 nm thick for SiO_2) with a deep-UV incoherent light source. If the subpixel lies within the SiO_2 substrate, its intensity is divided by the PEY ratio between TiO_2 and SiO_2. We note that the PEY ratio uses 1PPE PEY of each thin film, where we assumed the corresponding 2PPE yield at twice the wavelength has similar yield ratio. It would be ideal to determine the 2PPE yield ratio in place of one-photon photoemission. However, we were unable to measure the 2PPE yield ratio for the SiO_2 thin film due to a combination of sample charging and extremely low 2PPE PEY.

After calculating the intensity of each subpixel, we calculate the intensity of the parent pixel to be the average of the intensities of its subpixels. The processed x-y slices are then added together to represent the spatially resolved, IMFP-weighted integrated intensity in the z-direction. Finally, gaussian smoothing is applied (using smoothing distance of 25 nm to resemble the pixel size in PEEM images) to produce the 2-dimensional $|\boldsymbol{E}|^4$ image whose intensity is analogous to the photoemission intensity in PEEM images.

MEEP parameters:

In this section, we discuss the geometric parameters involved with modeling the unit cell of the metasurface simulated in MEEP. These parameters depart from the designed physical dimensions of the metasurface provided in Figure 1(d) in the main text and are meant to replicate the impact of the imperfections in the real metasurface [see SEM image Figure 1(e)]. Note while all physical dimensions simulated in MEEP (including the wavelength of the light source) are normalized to the lattice constant of the unit cell (300 nm) and therefore dimensionless, we will refer to all quantities using their un-normalized values.

The illuminating light source is a gaussian plane wave source located at a height of 1050 nm above the top of the meta-atom. The gaussian plane wave has a temporal full width at half maximum of 170 fs to be consistent with the pulse duration of the experimental light source (on the order of 10^2 fs, or ~1% frequency spread). The simulated light source can also be given any linear polarization [defined in Figure 1(b)] as well as angles that describe the incident light relative to the surface normal [defined in Figure 1(c)]. The values of incidence angles used to simulate each polarization are listed in Supporting Table S1.

Figure S7 illustrates the geometry of the metasurface modeled in the MEEP simulations (only one unit cell is simulated using periodic boundary conditions). Figure S7(a) is the top view of the

ideal meta-atom, with a perfectly circular shape with a diameter *d*. However, the circumference of the real meta-atom is highly irregular and displays many bumps and defects that break the meta-atom's rotational symmetry about the z-axis. Figure S7(b) illustrates how we model the imperfect circumference by "puncturing" small sections of the meta-atom edges with circles of diameter Δd. To maintain the same total area as the original circle of diameter *d* (which preserves the E_{ph} value at resonance), the new circle (outlined by the red line) is given a slightly larger diameter than *d* as calculated from *d* and Δd. In addition, we artificially suppress the intensity along the circumference not only because of the surface roughness but also because the strong electric field from the objective lens of the PEEM (~7 kV/mm) would pull electrons originating from the side walls of the meta-atoms radially away from the center, causing their intensity to be diffused as some background intensity. The uneven surface of the side walls makes the electric field non-trivial and difficult to model, so the simulated intensity from the edges was simply set to zero within a distance Δd from the edge (red circle). Figure S8 compares the PEEM image for E_{ph} = 2.78 eV and 0° polarization (a) to the simulated images in (b) and (c), showcasing the need for the circumference puncturing and intensity suppression. Figure S8(d) is a diagram of the unit cell and polarization. We see that Figure S8(b), which displays the image simulated using the circumference treatment, reproduces the PEEM image very well. On the contrary, Figure S8(c) simulated without the treatment shows high intensity along the edge of the meta-atom that are absent in the PEEM image. Thus, the simulations are more accurate when they account for the roughness and suppressed intensity at the meta-atom circumference.

Figure S7(c) depicts a side view of the meta-atom, describing further modifications to the metasurface. We model the meta-atoms not as perfect cylinders but ones with slanted walls making some angle α with respect to the z-axis (giving them a trapezoidal cross-section when cut in the x-z plane). The cylinder diameter *d* represents the diameter of the top of the meta-atom, meaning the radius at the base is slightly larger depending on α. The corners of the trapezoidal cross-section are also rounded off using small, right triangles with side length *w*. We found that the side wall angle and the corners did not impact the simulations in any significant way (within the values possible from the fabrication process), but we used this slanted wall geometry and rounded corners of the meta-atom geometry because they more accurately represent the meta-atoms of the metasurface used in the PEEM measurement. The values used in the simulations are α of 3° and *w* of 5 nm.

In addition, Figure S7(c) shows that the meta-atom is placed on top of additional layer of TiO_2 of thickness ρ to model the additional TiO_2 deposited via atomic layer deposition (ALD) over the metasurface to alleviate sample charging. Note that the modeled structure is slightly different in the location of the additional TiO_2 layer as it does not fully reflect the fabrication process of the meta-atom arrays [compare with Figure 1(d) in main text]. This layer further sits on top of an SiO_2 substrate that extends down the rest of the simulated volume (substrate is effectively infinite). The upper and lower interfaces of the additional TiO_2 layer between the meta-atoms mix with the adjacent material (vacuum at top and SiO_2 at the bottom) due to the roughness δ of the SiO_2 substrate. Such mixing causes the thin film's effective refractive index, n_{eff}, to change according to the equation:

$$n_{\text{eff}} = \frac{n_{\text{TiO}_2}(\rho - 2\delta) + n_{\text{SiO}_2}\delta + n_{\text{vacuum}}\delta}{\rho}.$$

The index of refraction of SiO_2 for any given photon energy was interpolated from values reported by Malitson.[6] The index of refraction of TiO_2 was measured via ellipsometry from a blanket thin film and is plotted as a function of photon energy in Figure S9. Because the index of refraction changes with the photon energy, the ratio $n_{\text{eff}}/n_{\text{TiO}_2}$ is not fixed and thus also depends on the photon energy. We used a roughness δ of 1 nm, which is consistent with the typical roughness of fused silica substrates commercially available. The values of roughness and all other parameters used for the metasurface geometry in the simulation are listed in Supporting Table S2.

Mode identification:

In this section, we describe the detailed characteristics of the two resonances evaluated using simulations. To confirm that the resonance measured in Figure 3 and visualized in Figure 4 corresponds to the two overlapping resonances that are part of the metasurface design, we first calculated the photonic band structure of the metasurface using a Python-based simulation package: the guided-mode expansion (GME) method via legume.[7] Figure S10(a) is the calculated photonic band structure of the ideal metasurface [see Figure 1(d)]. We note that legume calculations used a fixed value of index of refraction for TiO_2 (2.6 from Siefke[8]) and SiO_2 (1.4655 from Malitson[6]). The band structure reveals three resonances within the visible range at the Γ-point, highlighted by the dashed ovals. These resonances are typical of Fano resonances within photonic crystal slabs with a square lattice[9,10,11] and arise from Mie-type resonances in dielectric metasurfaces.[12] For convenience, we name the three resonances Fano A, B, and C in the order of increasing E_{ph} as labeled in Figure S10(a). Fano A resonance appears as a single mode (mode 0) occurring at 2.72 eV and has a Q-factor many orders of magnitude higher than the others, characteristic of a bound state in the continuum (BIC). The other two resonances are clusters of multiple, lower Q-factor modes located around 2.82 eV and 3.02 eV whose bands diverge from each other with increasing wave vector (i.e., moving away from Γ-point by increasing the incidence angle of light source). We further narrow down the resonances probed via PEEM by field visualization.

To visualize the resonances identified in the band structure calculated using legume and to isolate which resonance corresponds to that measured by PEEM, we simulated the resonances of the same, ideal metasurface with MEEP. MEEP simulated the ideal metasurface under incident light of 0° polarization with a narrow frequency spread (<0.25% of central frequency, which is narrower than ~1% spread of experimental light source). The narrow frequency spread ensures that any resonance would have a much stronger response than the non-resonant effects such that the resulting images correspond almost entirely to the electromagnetic field distribution of the resonances. When harmonic inversion[13] detects high-Q modes contributing to the electric fields within the simulation, the $|\boldsymbol{E}|^4$ intensity image is generated using the same method for the simulated images in Figure 4 (see the MEEP simulation section). We compared these simulated $|\boldsymbol{E}|^4$ images with the PEEM image at resonance for 0° polarization.

Figure S10(b) shows the PEEM image [same as Figure 4(a)(iii)] for comparison with simulations, where S10(b)(i) is the diagram of the unit cell and polarization, while S10(b)(ii) is the PEEM image. The dashed circles in Figure S10(b)(ii) highlight the intense features in the PEEM image to be compared with the MEEP simulation. Figure S10(c) displays the simulated $|\boldsymbol{E}|^4$ image of Fano A resonance (BIC at 2.72 eV in legume band structure but occurs at 2.79 eV in MEEP), which is an electric quadrupole (EQ) mode. We note that because the electric field of the BIC has a 180° rotational symmetry about the z-axis, the simulated meta-atom needed to be slightly altered to break its 180° rotational symmetry for the simulated plane wave to couple with the mode. The $|\boldsymbol{E}|^4$ intensity distribution of the BIC has a 4-fold symmetry and is inconsistent with the 2-fold symmetry of the PEEM image [Figure S10(b)(ii)]. The field pattern of Fano A did not appear at any photon energy measured by PEEM (see Supporting Information Movies). We do not expect to see this mode as it consists primarily of $\boldsymbol{E}_z$, whereas the illuminating light source at near-normal incidence has almost no $\boldsymbol{E}_z$ component and thus would not couple with the mode. In contrast to Fano A, the field distribution of Fano B resonance shown in Figure S10(d) agrees with that measured by PEEM. Fano B resonance consists of electric dipole (ED) modes whose fields are concentrated around the edge and exterior of the meta-atom as highlighted by the dashed circles. Fano C resonance at 3.02 eV was ruled out because it has a Q-factor too low (<10) to be detected by harmonic inversion. We therefore conclude that one of the resonances contributing to the PEEM measurements is that of Fano B resonance, a cluster of ED modes around 2.82 eV. As an additional measure to verify these findings, the same MEEP simulations with harmonic inversion were performed for plane waves of 42° polarization (not shown) for Fano A and B resonances. The resulting $|\boldsymbol{E}|^4$ intensity distributions agree with the PEEM image of the same polarization at resonance.

Because the Fano resonance accounts for only one resonance with its electric field concentrated around the edge and exterior of the meta-atom [Supporting Figure S10(b) and (d)], we investigate the $|\boldsymbol{E}|^4$ distribution simulated using MEEP in more detail. Figure S11(a)-(c)(i) show the simulated images of the metasurface for 0° polarization (red arrow) at 2.83, 2.78, and 2.73 eV, respectively. The simulation is the same as the one used to generate the simulated images in Figure 4(a). Here instead of a top-down (x-y) perspective, we view the $|\boldsymbol{E}|^4$ intensity in the y-z cross section at $x = 0$. The intensity profiles across the white, dashed lines in (i) are plotted in Figure S11(a)-(c)(ii), where depth of 0 corresponds to the top of the meta-atom and ~80 nm corresponds to the bottom. The red circles in (i) highlight an intense electric field location whose position along the z-axis (depth) changes as a function of E_{ph}. This movement is corroborated by the intensity profiles in (ii). Because the feature changes purely in the z-direction, it cannot be affected by the metasurface lattice, whose periodicity is purely in the x-y plane. Thus, it is not a Fano resonance and does not appear in the legume band structure [Figure S10(a)]. Instead, we determine this feature to be a Fabry-Pérot (FP) resonance[14] caused by phase-matching between the reflected waves from the top and bottom faces of the meta-atoms. This constructive interference results in the 2.73 eV shoulder in the reflection spectrum in Figure 3(a) in the main text. However, as the phase-matching condition does not apply within the meta-atom itself (only the boundary), constructive interference does not occur inside the meta-atom and contributes to the weaker 2.73 eV shoulder in the PEEM spectra in Figure 3(b). The FP resonance manifests as the intensity at the center of all PEEM and simulated images in Figure 4 and S3.

In summary, we identified the two overlapping resonances using two methods. First, we calculated the band structure of the metasurface with legume and identified the three Fano resonances (A, B, C). Comparison of the simulated field distributions of each Fano resonance via MEEP with PEEM images showed that PEEM had imaged only the Fano B resonance. Second, we examined the cross-sections of the MEEP simulations in the y-z plane, which revealed a Fabry-Pérot (FP) resonance that moves purely in the z-direction and unaffected by the metasurface periodicity in the x and y-directions. We thereby confirm that the single resonant feature measured experimentally in Figure 3 and 4 is the result of the overlap between Fano B and Fabry-Pérot resonances.

Details on IMFP extraction:

Here we discuss in detail about IMFP extraction beyond what was discussed in the main text, including fitting simulations to the PEEM data. Extraction of IMFP from the PEEM data involves a hyperspectral analysis to compare areas of different photoemitting thicknesses, similar to a previous photoemission study.[4] For the metasurface in our study, the different photoemitting areas are the interior and exterior of the meta-atom [as defined by Figure 2(a)(i)]. The choice of comparing the intensity features in the interior and exterior (via intensity ratio) is corroborated by singular value decomposition (SVD) of the images. Performing SVD isolates various features of the image (we will call them eigen-images to be analogous to eigenvectors), with greater singular values corresponding to features that have greater contribution. Thus, comparing the significant eigen-images (largest singular values) to various parts of the simulated offers an alternative method to extract the IMFP. As such, we performed SVD on the PEEM images and found that the most significant eigen-image almost entirely replicates the PEEM images themselves. The second-most significant eigen-image has a singular value that is much smaller than the largest singular value and has very little resemblance to any intensity feature of the PEEM. Most importantly, the most significant eigen-image follows the switching of intensity concentration from the interior to the exterior as E_{ph} is increased. This behavior of the eigen-image suggests that the intensity features of greatest significance are the intensities at the interior and exterior of the meta-atom. Performing SVD on the simulated images return similar results in that only one singular value is significant and corresponds to the interior or exterior intensity features. Therefore, we conclude that a hyperspectral analysis involving the ratio of intensity between the meta-atom interior and exterior is a valid approach to extracting the IMFP.

Next, we present details on the intensity ratio calculation and the IMFP fitting procedure. To alleviate the coarseness of the meta-atom boundary in the images due to the pixel resolution (PEEM images are ~22 pixels per unit cell laterally, while simulated images are 34 pixels), each pixel was divided into 7-by-7 subpixels (results converge at as low as 3-by-3 subpixels). Each subpixel was then evaluated to be either in the interior or exterior based on its distance from the meta-atom center. Depending on the evaluated location of the subpixel, the intensity value of the parent pixel would be added to the total interior or exterior intensity. This evaluation was performed for each PEEM and simulated dataset to obtain the total interior and exterior

intensities as a function of E_{ph} and therefore the intensity ratio as a function of E_{ph} presented in Figure 6.

Fitting the simulated intensity ratio to the PEEM intensity ratio could not be performed automatically. Each simulated dataset takes multiple days to generate, making an iterative fitting process unfeasible. Instead, datasets were simulated using different IMFP values in increments of 5 nm, and each intensity ratio curve was compared to the PEEM intensity ratios. The simulated dataset for IMFP of 35 nm lay closest to the middle of the PEEM datapoints at the higher E_{ph} side of the 2.76 eV resonance peak. Likewise, simulations for 25 and 45 nm lay closest to the upper and lower boundaries of the PEEM datapoints and were chosen to represent the lower and upper bounds of the IMFP. Fitting to the higher E_{ph} side was prioritized due to the stronger-than-expected Fano features on the low E_{ph} side. This inaccuracy is likely due to a combination of modeling errors, which includes not accounting for the sharp increase in IMFP that is expected as electron energy approaches zero. Higher values of IMFP (~50-60 nm) are required to fit the simulated intensity ratios on the low E_{ph} side. However, doing so results in the image at resonance becoming highly inaccurate both visually and by intensity ratio comparison (interior intensity becomes too high). Therefore, we determined that fitting IMFP to the higher E_{ph} side worked best for producing simulated images that best reproduced the prominent features of PEEM images including the intensity profiles and spectral shape.

Supporting Figures:

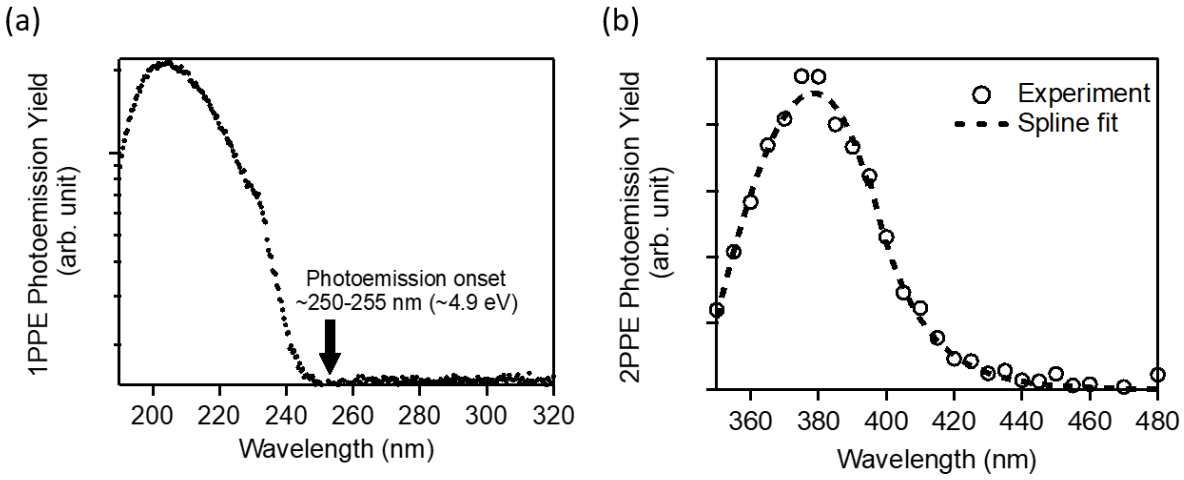

Supporting Figure S1. (a) 1PPE photoemission yield of a 46nm TiO_2 thin film as a function of photon wavelength showing onset at approximately 250-255 nm (4.9 eV). (b) 2PPE photoemission yield of the 46 nm TiO_2 thin film as a function of photon wavelength, divided by the square of laser power.

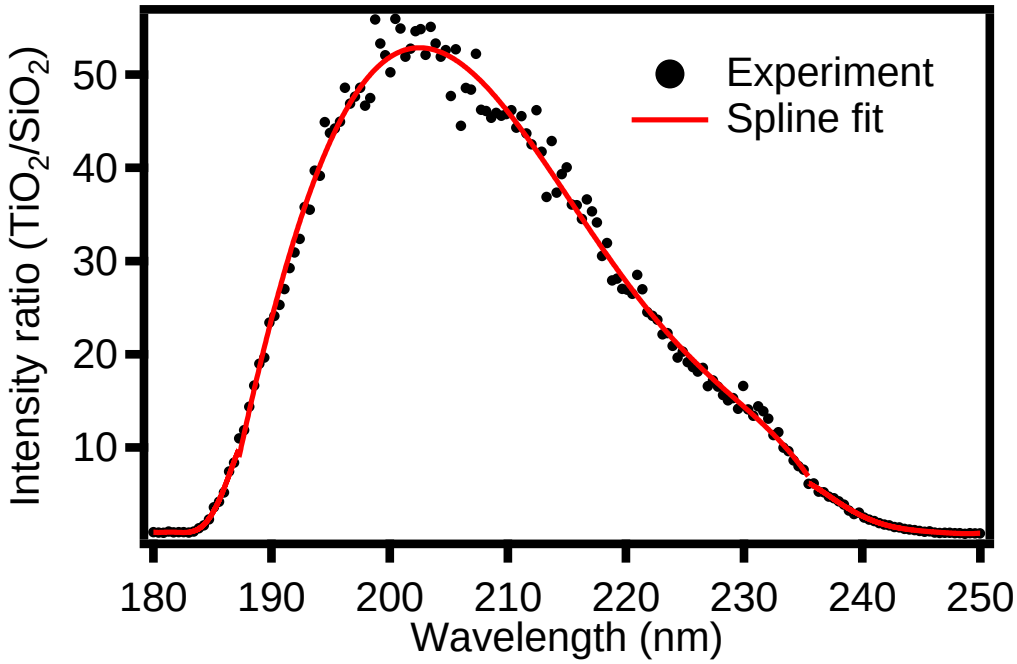

Supporting Figure S2. Ratio of photoemission intensity between TiO_2 and SiO_2 thin films as a function of photon wavelength measured using incoherent, deep UV-visible light source, displayed with a spline fit.

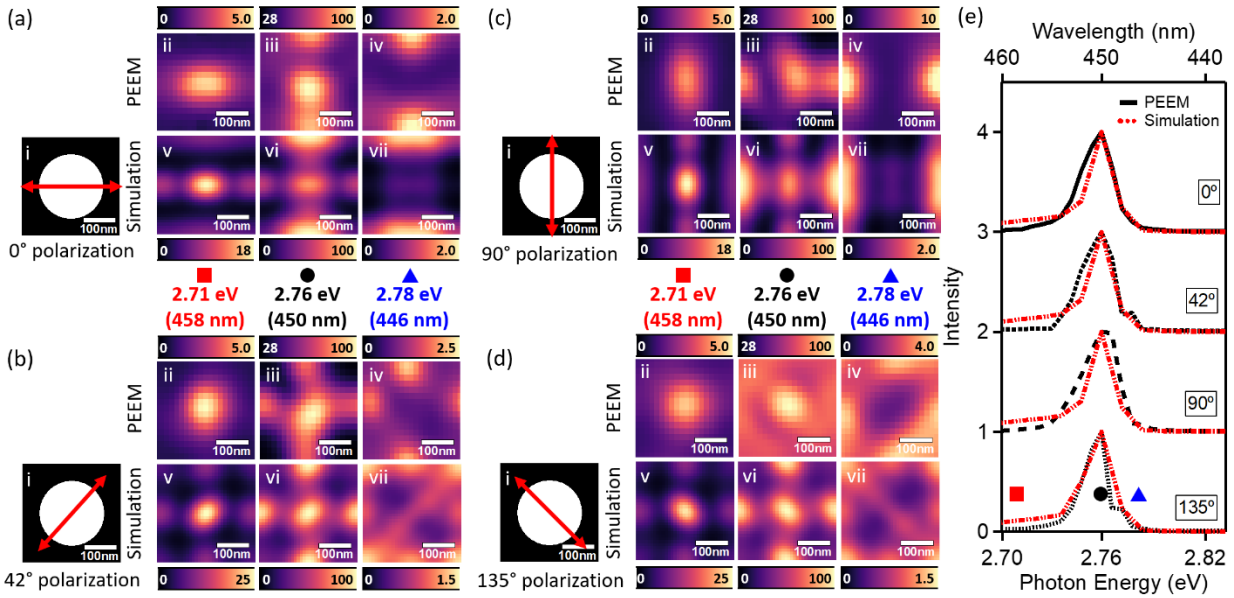

Supporting Figure S3. The PEEM photoemission intensity images of one unit cell of the metasurface are compared with the corresponding simulated $|\boldsymbol{E}|^4$ images for (a) 0°, (b) 42°, (c) 90°, and (d) 135° polarizations. In (a), (b), (c), and (d), images (i) display the unit cell diagram with polarization represented by the red arrow. Images (ii), (iii), and (iv) are the PEEM images at E_{ph} of 2.71, 2.76, and 2.78 eV, respectively, while images (v), (vi), and (vii) are the simulated $|\boldsymbol{E}|^4$ images at 2.76, 2.81, and 2.83 eV, respectively [shifted to lower photon energy by ~0.05 eV (8 nm) to line up with PEEM images]. (e) Plots of the simulated $|\boldsymbol{E}|^4$ spectra alongside the corresponding PEEM spectra as a function of photon energy for all four polarizations (all spectra but 135° are offset vertically for clarity). The colored shapes in (e) mark the photon energies for which the PEEM and simulated images in (a), (b), (c), and (d) are displayed.

Polarization direction	Polar angle θ	Azimuthal angle φ
0°	0.05°	270°
42°	0.15°	130°
90°	0.05°	20°
135°	0.1°	310°

Supporting Table S1. The polar and azimuthal angles of incident light simulated in MEEP for each polarization. See Figure 1(c) in main text for the definitions of the angles.

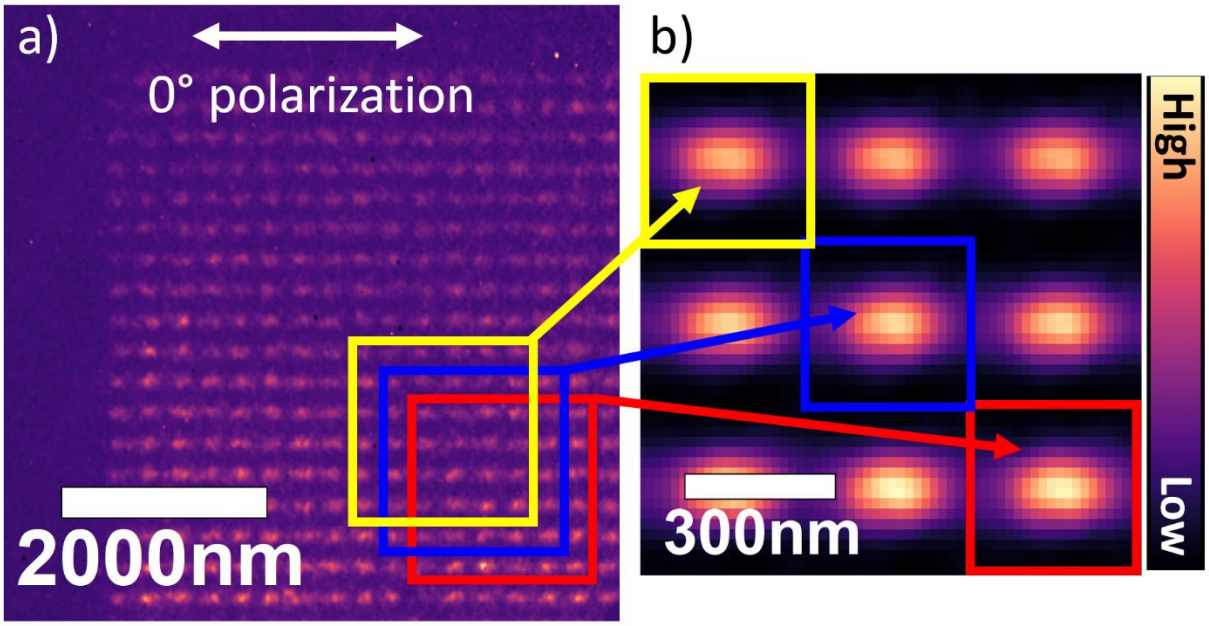

Supporting Figure S4. (a) PEEM image of the metasurface at 10 μm field of view at E_{ph} of 2.7 eV for 0° polarization. The colored boxes surround the meta-atoms that were summed to produce (b) the accumulated meta-atom image (also boxed with corresponding colors).

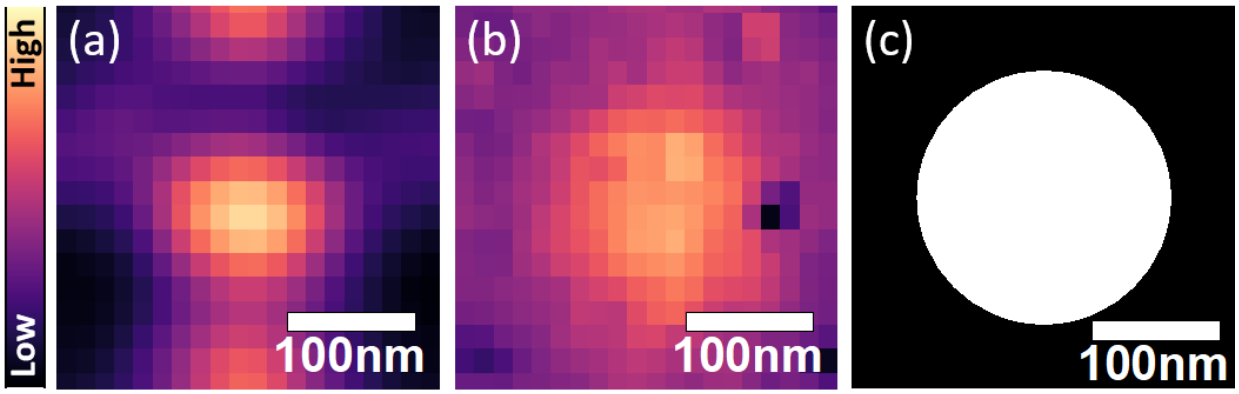

Supporting Figure S5. (a) PEEM image of one unit cell illuminated at photon energy of 2.76 eV for 0° polarization. (b) The same unit cell illuminated by an incoherent light source at photon energy of 6.20 eV. (c) Diagram of the unit cell, with the white circle representing the meta-atom interior and the black area representing the exterior.

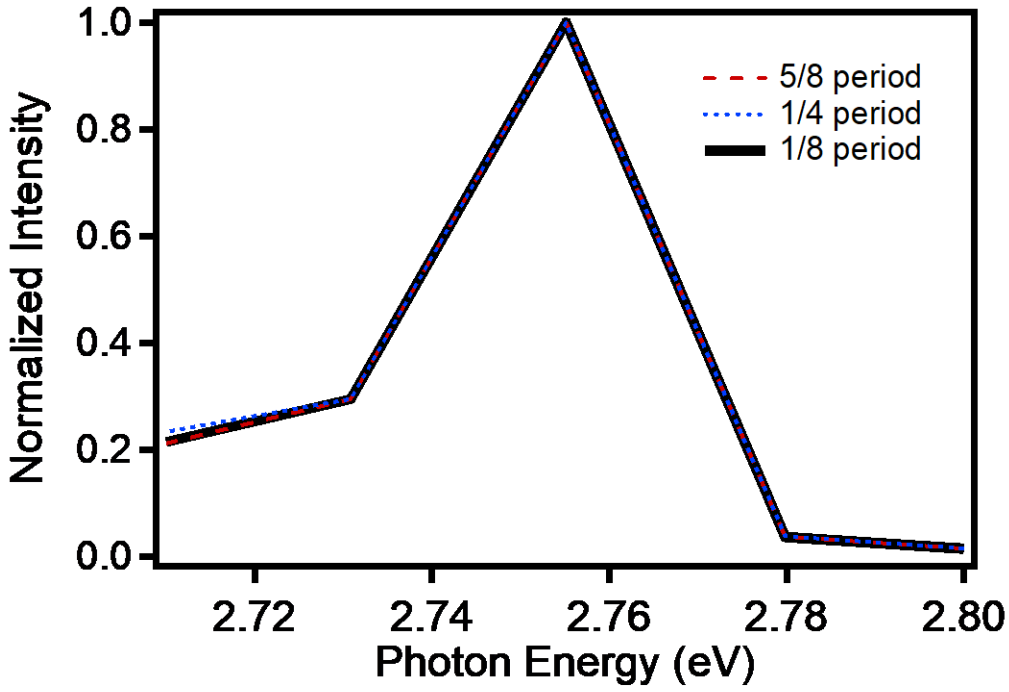

Supporting Figure S6. Normalized spectra of simulated $|\boldsymbol{E}|^4$ images of one unit cell for 0° polarization plotted for different time-integration steps (every 1/8, 1/4, and 5/8 oscillation period) showing that the result from integrating in 5/8 period timesteps is nearly identical to that of 1/8 period timesteps.

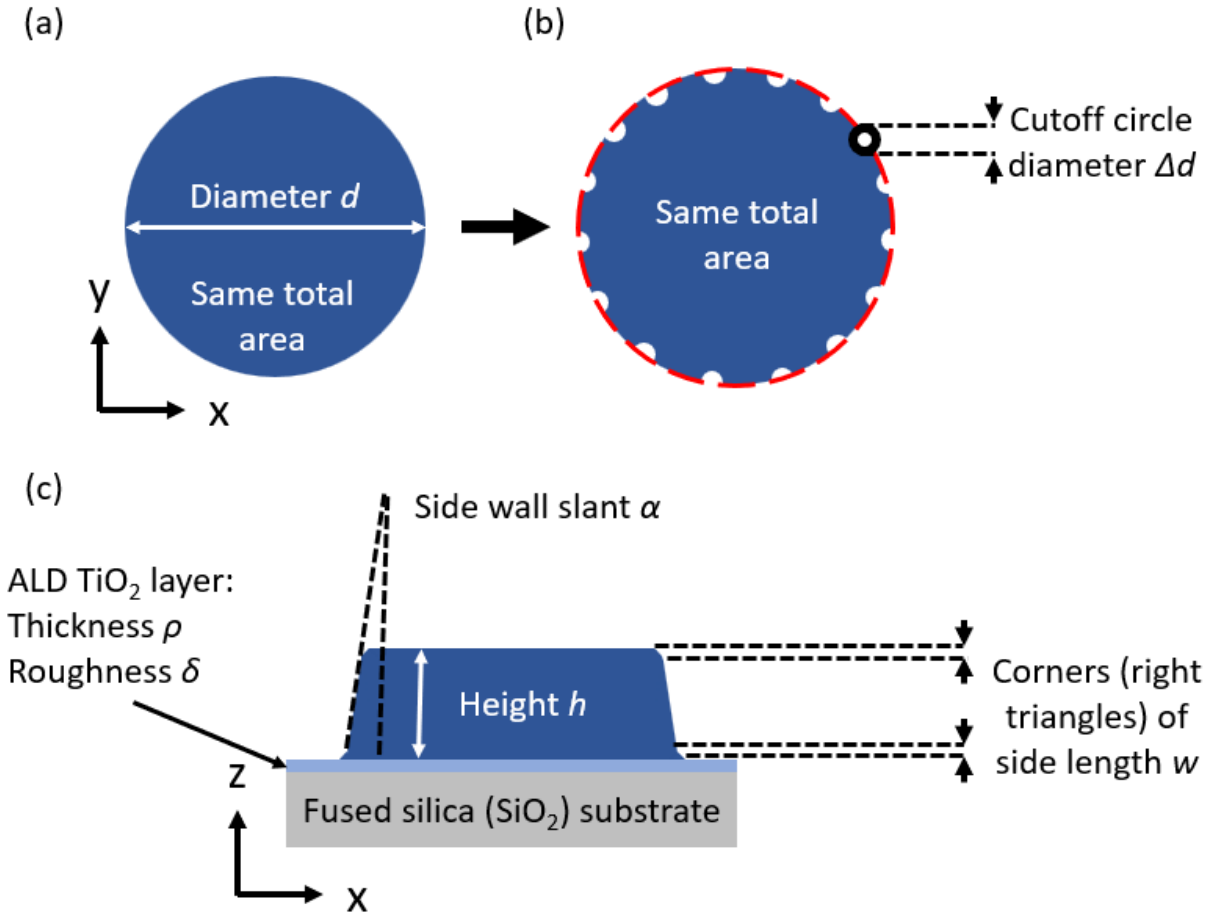

Supporting Figure S7. Diagram of the metasurface modeled in MEEP. (a) The ideal meta-atom is a perfect cylinder of diameter *d*. (b) To simulate the uneven circumference of the real meta-atoms, the meta-atom is "punctured" at the edges using cutoff circles of diameter Δd. The new pseudo-cylinder's radius is adjusted to maintain the same total area. (c) Side view of the modeled structure of the metasurface unit cell, showing additional parameters. The meta-atom has a height *h* and sits on top of a thin film of thickness ρ whose surface roughness δ causes it to have an effective index of refraction n_{eff} below that of pure TiO_2. The meta-atom is also given slanted side walls making an angle of α with respect to the z-axis as well as corners that have a slant of 45° with respect to the z-axis and side length *w*. The values for the other parameters used in the simulation are provided in Supporting Table S2. Note that the modeled structure is slightly different in the location of the ALD TiO_2 layer as it does not fully reflect the fabrication process of the meta-atom arrays.

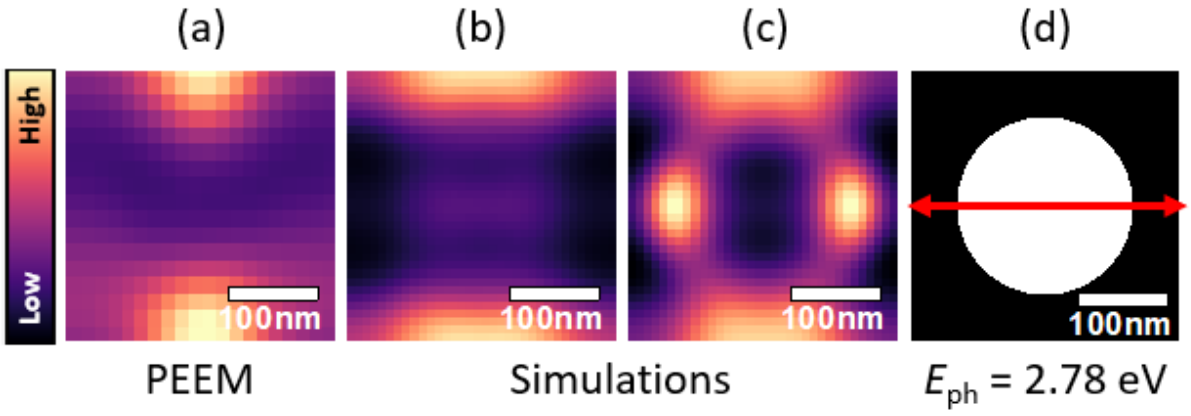

Supporting Figure S8. Images of the metasurface unit cell for E_{ph} = 2.78 eV and 0° polarization from (a) PEEM, (b) simulation with the meta-atom circumference treatment described in Figure S7(b), and (c) simulation without the treatment. (d) Diagram of the ideal unit cell, with the white circle representing the meta-atom interior and the red arrow representing the polarization.

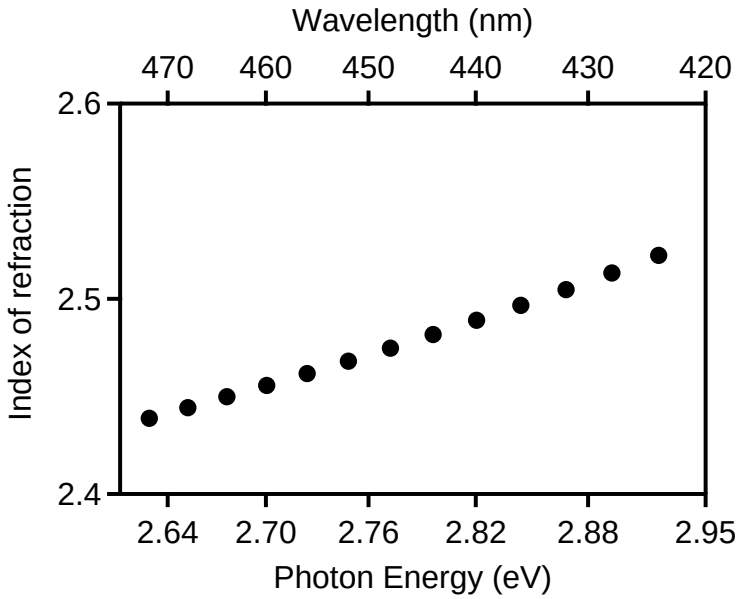

Supporting Figure S9. Index of refraction of a TiO_2 thin film as a function of photon energy as measured by ellipsometry. The indices of refraction used in the simulations were interpolated from this measurement.

Parameter	Value
Diameter d	105 nm
Cutoff Δd	7.5 nm
Thickness ρ	10 nm
Roughness δ	1 nm
Side wall slant α	3°
Height h	83 nm
Corner side length w	5 nm

Supporting Table S2. Values of modeling parameters defined in Figure S7 and used to generate the MEEP images in Figure 4 and S3.

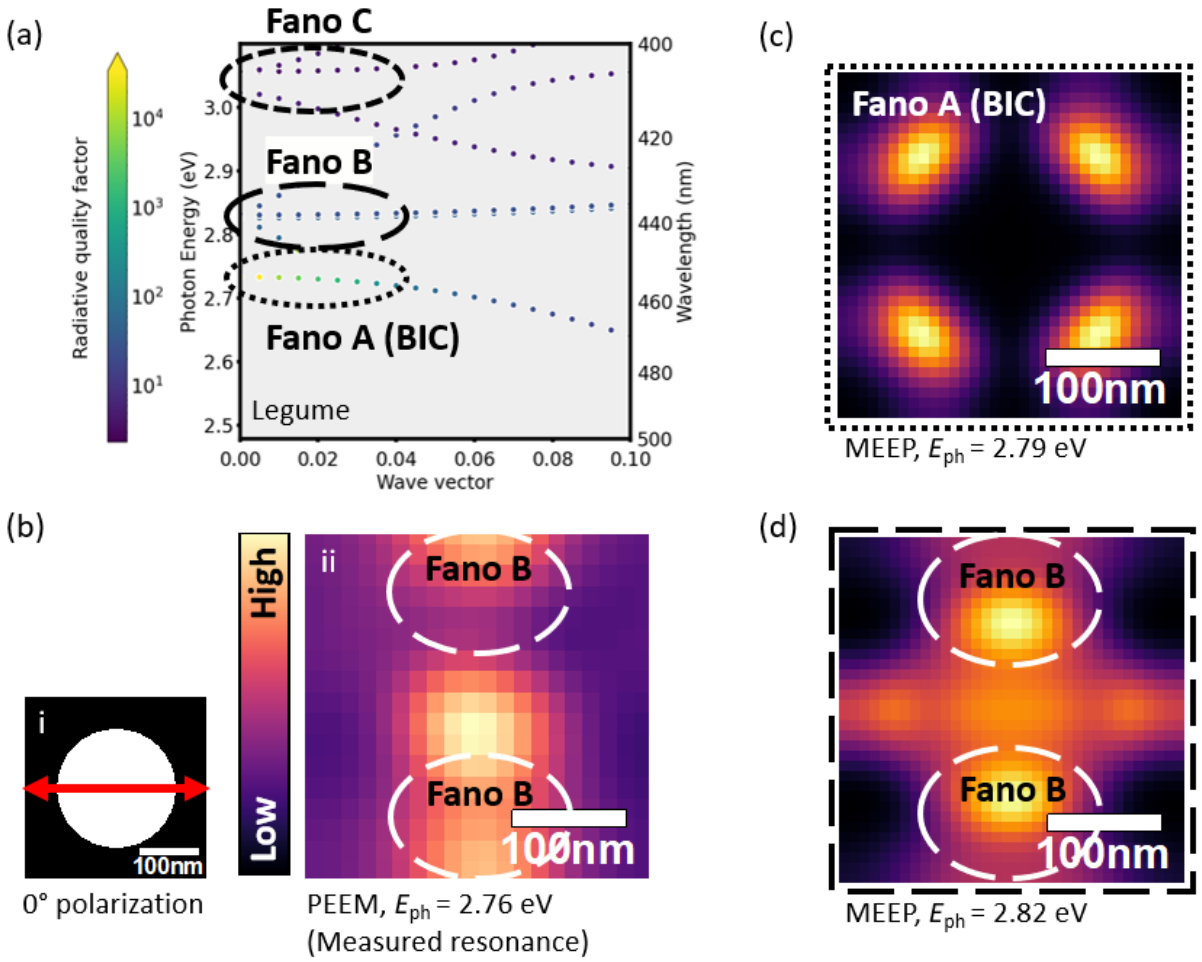

Supporting Figure S10. (a) Band structure of the ideal metasurface as calculated by legume, showing three Fano resonances in the wavelength range of interest (2.4 to 3.1 eV). (b) (i) Unit cell diagram representing the 0° polarization (red arrow) for (ii) the PEEM photoemission intensity map of one unit cell of the metasurface at resonance of 2.76 eV. (c) Simulated $|\boldsymbol{E}|^4$ map of one unit cell of the metasurface of displaying the high-Q, Fano A mode (BIC) at photon energy of 2.79 eV. (d) MEEP simulation of $|\boldsymbol{E}|^4$ map of one unit cell of the metasurface of the cluster of modes at photon energy of 2.82 eV. In (b) and (d), dashed circles are drawn around field patterns associated with Fano B resonance.

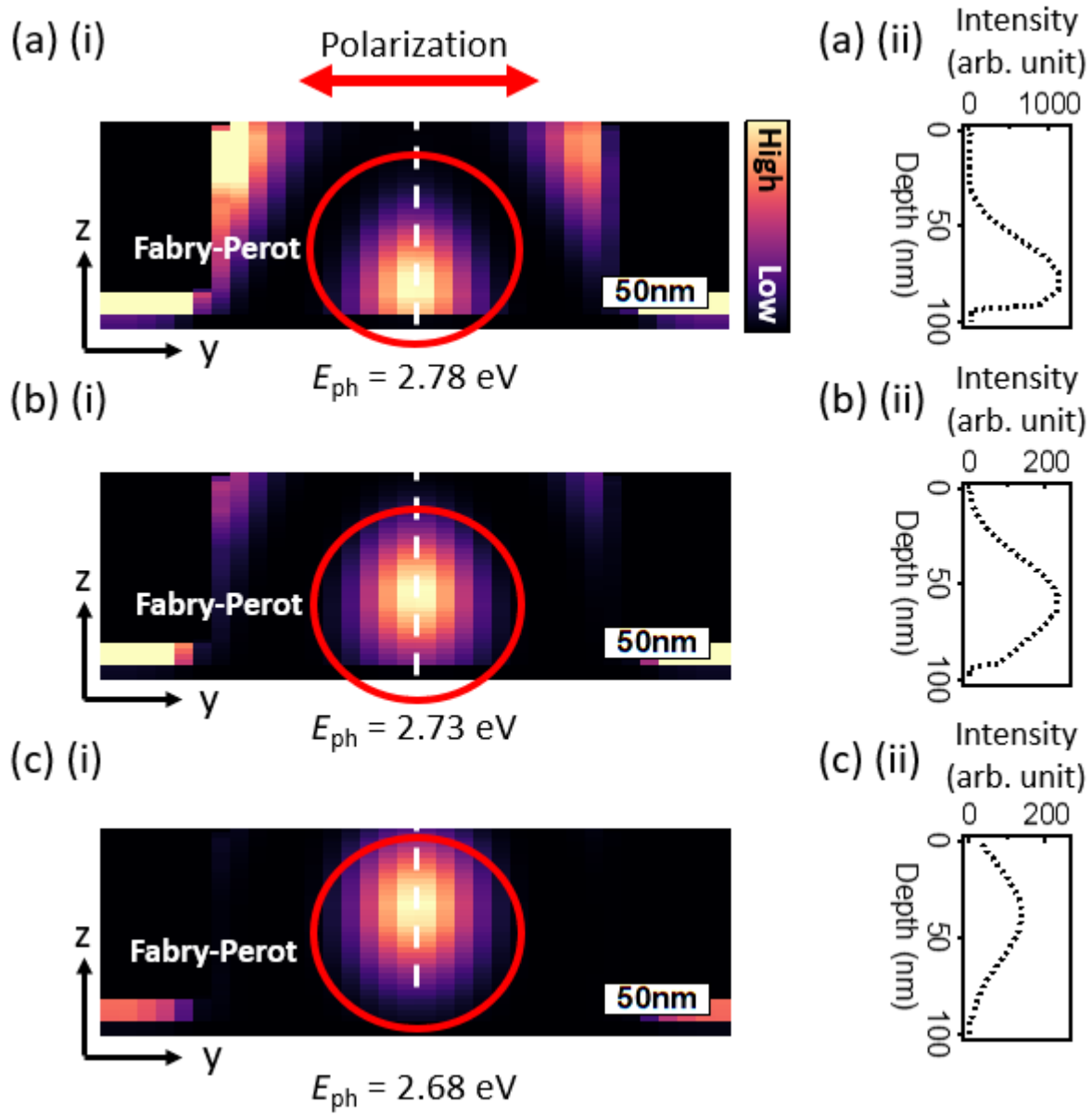

Supporting Figure S11. Evolution of Fabry-Pérot resonance for 0° polarization (red arrow) visualized via MEEP simulation. In (a), (b), and (c), the images labeled (i) show cross-sections of the $|\boldsymbol{E}|^4$ map in the y-z plane at x = 0 for photon energies of 2.78 eV, 2.73 eV, and 2.68 eV, respectively. Images (ii) show the profile of $|\boldsymbol{E}|^4$ intensity taken across the white dashed line in the corresponding cross-sectional images (i), where the depth 0 nm corresponds to the top of the meta-atom. The Fabry-Pérot resonance features are marked in images (i) by the red solid circles.

References for Supporting Information

[1] H. Ueba, B. Gumhalter, *Prog. Surf. Sci*. **2007**, *82*, 193.

[2] N. V. Tkachenko, *Optical Spectroscopy: Methods and Instrumentations*, Elsevier, Oxford, UK **2006**.

[3] A. Kubo, K. Onda, H. Petek, Z. Sun, Y. S. Jung, H. K. Kim, *Nano Lett*. **2005**, *5*(6), 1123.

[4] A. Boehm, S. D. Gennaro, C. F. Doiron, T. E. Beechem, M. B. Sinclair, I. Brener, R. Sarma, T. Ohta, *APL Photonics* **2024**, *9*, 066103.

[5] A. F. Oskooi, D. Roundy, M. Ibanescu, P. Bermel, J. D. Joannopoulos, S. G. Johnson, *Comput. Phys. Commun.* **2010**, *181*, 687.

[6] I. H. Malitson, *J. Opt. Soc. Am.* **1965**, *55*, 1205.

[7] M. Minkov, I. A. D. Williamson, L. C. Andreani, D. Gerace, B. Lou, A. Y. Song, T. W. Hughes, S. Fan, *ACS Photonics* **2020**, *7*, 1729.

[8] T. Siefke, S. Kroker, K. Pfeiffer, O. Puffky, K. Dietrich, D. Franta, I. Ohlídal, A. Szeghalmi, E.-B. Kley, A. Tünnermann, *Adv. Opt. Mater.* **2016**, *4*, 1780.

[9] J. D. Joannopoulos, S. G. Johnson, J. N. Winn, R. D. Meade, *Photonic Crystals: Molding the Flow of Light (second edition)*, Princeton University Press, Princeton, NJ **2008**.

[10] J. Lee, B. Zhen, S.-L. Chua, W. Qiu, J. D. Joannopoulos, M. Solijačić, O. Shapira, *Phys. Rev. Lett.* **2012**, *109*, 067401.

[11] S. Fan, *Phys. Rev. B* **2002**, *65*, 235112.

[12] T. Liu, R. Xu, P. Yu, Z. Wang, J. Takahara, *Nanophotonics* **2020**, *9*(5), 1115.

[13] V. A. Mandelshtam, H. S. Taylor, *J. Chem. Phys*. **1991**, *107*, 6756.

[14] A. A. Bogdanov, K. L. Koshelev, P. V. Kapitanova, M. V. Rybin, S. A. Gladyshev, Z. F. Sadrieva, K. B. Samusev, Y. S. Kivshar, M. F. Limonov, *Adv. Photonics* **2019**, *1*(1), 016001.